New Journal of Physics
The open access journal at the forefront of physics

Deutsche Physikalische Gesellschaft DPG
IOP Institute of Physics

Published in partnership with: Deutsche Physikalische Gesellschaft and the Institute of Physics

OPEN ACCESS

RECEIVED
12 November 2021

REVISED
28 December 2021

ACCEPTED FOR PUBLICATION
11 January 2022

PUBLISHED
9 February 2022

PAPER

Ultrafast modulation of vibrational polaritons for controlling the quantum field statistics at mid-infrared frequencies

Johan F Triana[1,*] **and Felipe Herrera**[1,2,*]

[1] Department of Physics, Universidad de Santiago de Chile, Av. Víctor Jara 3493, Estación Central, Santiago, Chile
[2] ANID—Millennium Science Initiative Program, Millennium Institute for Research in Optics, Chile
[*] Authors to whom any correspondence should be addressed.

E-mail: johan.triana@usach.cl and felipe.herrera.u@usach.cl

Keywords: molecular polaritons, quantum light, mid-infrared resonators, molecular vibrations, cavity QED, quantum squeezing, ultrastrong coupling

Abstract

Controlling the quantum field statistics of confined light is a long-standing goal in integrated photonics. We show that by coupling molecular vibrations with a confined mid-infrared cavity vacuum, the photocount and quadrature field statistics of the cavity field can be reversibly manipulated over sub-picosecond timescales. The mechanism involves changing the cavity resonance frequency through a modulation of the dielectric response of the cavity materials using femtosecond UV pulses. For a single anharmonic molecular vibration in an infrared cavity under ultrastrong coupling conditions, the pulsed modulation of the cavity frequency can adiabatically produce mid-infrared light that is simultaneously sub-Poissonian and quadrature squeezed, depending on the dipolar behavior of the vibrational mode. For a vibration-cavity system in strong coupling, non-adiabatic polariton excitations can be produced after the frequency modulation pulse is over, when the system is initially prepared in the lower polariton state. We propose design principles for the generation of mid-infrared quantum light by analyzing the dependence of the cavity field statistics on the shape of the electric dipole function of the molecule, the cavity detuning at the modulation peak and the anharmonicity of the Morse potential. Feasible experimental implementations of the modulation scheme are suggested. This work paves the way for the development of molecule-based mid-infrared quantum optical devices at room temperature.

1. Introduction

Quantum light sources are key to the success of optical quantum technologies [1]. In the visible spectral range, several mechanisms are available to produce quantum light, such as single photon emission by atoms in optical resonators [2, 3], photon blockade in cavity optomechanics [4], or ensemble strong coupling with atomic emitters [5]. In the near infrared (0.7–2.5 μm), quantum light generation is a mature technology that has become the workhorse for applications in quantum communication [6, 7] and sensing [8, 9]. Quantum-efficient semiconductor [10] and superconductor [11] photodetectors are broadly available in this frequency range. In contrast, quantum optical tools in the mid-infrared spectral region (2.5–25 μm) are much less developed [12, 13]. Quantum cascade lasers have been used to produce mid infrared quantum light [14] and early demonstrations of quantum light detection in this frequency regime are available [15, 16].

In this work, we introduce a new mechanism for the deterministic generation and dynamical manipulation of quantum light in the mid-infrared frequency range. The mechanism involves ultrafast modulation of the confined mid infrared vacuum field under strong and ultrastrong light–matter coupling. Strong vibration-cavity coupling has been demonstrated with Fabry–Perot cavities [17–25], plasmonic resonators [26, 27], van der Waals resonators [28] and polar dielectric resonators [29]. Ultrastrong coupling

[30, 31] has also been demonstrated in the mid-infrared [32–34]. The proposed modulation of the light–matter dynamics is based on the transient modification of the dielectric function of the materials that confine the infrared vacuum by driving interband transitions with a driving source. The associated change in boundary conditions for the electromagnetic field results in a parametric change of the cavity vacuum frequency that is related with the dynamical Casimir effect [35]. This frequency modulation mechanism has been demonstrated for mid-infrared resonators using electrical [36], chemical [37] or electromagnetic [38, 39] driving sources.

We consider a scheme where the mid infrared cavity frequency $\omega_c \approx 1840$ cm^{-1} (5.6 μm) is modulated over sub-picosecond (ps) timescales by 200–400 cm^{-1} using a single femtosecond UV pulse that drives a target cavity boundary material to transiently modify its carrier density. Our analysis implies a cavity scenario where the active molecular medium is a single anharmonic molecular vibrational resonance in the ground electronic state, protected by materials design from the strong UV driving source. Any residual electronic excitation after photoprotection should not deplete the ground vibrational levels significantly. We show that the photocount and quadrature field statistics of the infrared cavity field is transiently modified by the frequency modulation pulse and correlate the predicted changes with the intrinsic properties of the molecular vibration and the light–matter interaction process. Our results are expected to be valid for single-molecule systems with frequency modulation timescales shorter than the characteristic polariton relaxation times, which for high-quality infrared nanoresonators can reach the few ps regime [28].

The article is organized as follows: in section 2, we review the theoretical framework for cavity quantum electrodynamics with anharmonic molecular vibrations, and the numerically methods used for unitary wavepacket propagation. We also review the relevant concepts of quantum field statistics. We study the evolution of the intracavity field statistics for a Gaussian frequency modulation in vibrational ultrastrong coupling (VUSC) in section 3 and discuss strong coupling in section 4. In section 5, we study the effect of vibrational anharmonicity. We conclude and discuss possible experimental realizations in section 6.

2. Methodology

2.1. MLQR model with cavity frequency modulation

We model light–matter interaction of a confined cavity mode of frequency ω_c with a single anharmonic vibration mode of fundamental frequency ω_v in the mid-infrared as a Morse oscillator using the multi-level quantum Rabi (MLQR) model [40, 41], recently developed to consistently describe the strong and ultrastrong vibration-cavity coupling regimes in the electric dipole approximation [42]. Taking into account the possible time-dependence of the cavity frequency due to external UV pulse driving, the corresponding MLQR Hamiltonian can be written in coordinate space as (in atomic units)

$$\hat{\mathcal{H}}(t) = \hat{H}_M - \frac{1}{2}\frac{\partial^2}{\partial \hat{x}^2} + \frac{1}{2}\omega_c(t)^2\hat{x}^2 + \sqrt{2\omega_c(t)}\mathcal{E}_0(t)\hat{d}(q)\hat{x}, \tag{1}$$

where the vibrational Hamiltonian $\hat{H}_M$ includes the nuclear kinetic energy $\hat{T}(q)$ and the potential energy $\hat{V}(q)$ along the mass-weighted normal mode coordinate q. The second and third terms describe the quantized cavity oscillator with quadrature operator $\hat{x}$ and frequency $\omega_c(t)$. The last term is the electric dipole light–matter coupling, proportional to the amplitude of the vacuum fluctuations at the cavity frequency $\mathcal{E}_0(t) = \lambda_g\omega_c(t)/d_{10}$.

The light–matter coupling strength is given in terms of the dimensionless parameter λ_g, which is equivalent to the conventional Rabi coupling ratio g/ω_c [30, 31] for $g \equiv \langle 1|\hat{d}(q)|0\rangle\mathcal{E}_0$, where $|0\rangle$ and $|1\rangle$ are the ground and first excited vibrational levels, $\hat{d}(q)$ is the electric dipole function [43] and $d_{10} = \langle 1|\hat{d}(q)|0\rangle$. The onset of the conventional ultrastrong coupling regime is thus reached when $\lambda_g \sim 0.1$ [31]. Strong coupling implies $\lambda_g \gtrsim 0.01$.

Under UV pulse driving, the cavity frequency is taken to vary according to a Gaussian function as

$$\omega_c(t) = \omega_c\left(1 + \eta e^{-(t-t_d)^2/2\tau^2}\right), \tag{2}$$

where the undriven cavity frequency being resonant with the fundamental vibration frequency ($\omega_c(0) = \omega_v$). As anticipated above, we assume the cavity frequency shifts at the UV pulse peak by up to 20% ($\eta = \pm 0.2$), red-detuned (minus sign) or blue-detuned (plus sign) relative to the undriven resonance frequency. According to equation (1), the frequency modulation not only changes the vibration-cavity detuning, but also the light–matter interaction strength. In terms of the vacuum Rabi frequency $g = d_{10}\sqrt{\omega_c/2\epsilon V}$, where ϵ is the frequency-independent dielectric constant and V the quantization volume, cavity frequency modulations of 20% correspond to changes in g of about 10%. These Rabi coupling

Table 1. Parameters of Morse potential energy curves [equation (3)] and dipole moment functions [equation (4)] employed in this work and plotted in figure 1.

	D_e (eV)	α (a.u.)	q_{eq} (Bohr)	Δ_{21} [cm^{-1}]
$V_A(q)$	6.80	1.50	4.0	31.9
$V_B(q)$	9.80	1.25	4.0	22.1
	d_0 [Debye]	q_0 [Bohr]	q_1 [Bohr]	σ Bohr
$d_{NP}(q)$	5.08	4.0	4.0	0.6
$d_{PR}(q)$	2.54	2.7	4.5	0.6

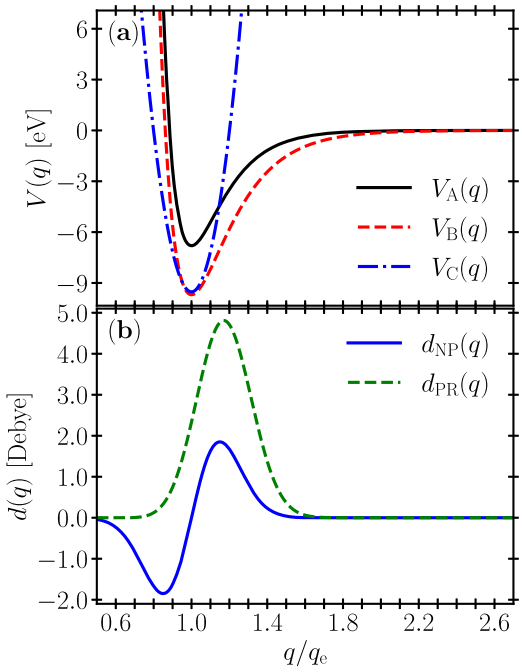

Figure 1. Vibrational potentials and dipole functions. (a) Morse potentials V_A (solid line) and V_B (dashed line) along the normal mode coordinate q. The harmonic oscillator potential V_C (dot-dashed line) with the same ω_v is also shown. In all cases, the reduced mass is $\mu = 8.5$ AMU and the fundamental frequency is $\omega_v \approx 1838$ cm^{-1}. (b) Dipole moment functions $d(q)$ for polar-right (dashed line) and a non-polar vibrational modes (solid line).

fluctuations could in principle be measured using transient infrared cavity absorption spectroscopy [21, 24]. Throughout this work, we assume the pulse is centered at $t_d = 250.0$ fs and the width parameter is $\tau = 62.5$ fs (FWHM = 147 fs).

2.2. Dipolar Morse oscillator

To understand the influence of the spectral anharmonicity and the dipolar structure of molecular vibrations on the unitary evolution of the frequency-modulated cavity field, we combine three different vibrational potentials $V(q)$ and two dipole moment functions $d(q)$ to search for conditions that are most effective at producing dramatic changes in the quantum field statistics of the infrared field.

For anharmonic vibrations we use the Morse potential [44]

$$V(q) = D_e(1 - e^{-\alpha(q-q_{eq})})^2 - D_e, \tag{3}$$

where D_e is the classical dissociation energy, q_{eq} the equilibrium mode coordinate, and α the anharmonicity parameter. For $\alpha \ll 1$, the Morse potential can be accurately truncated at second order in q, giving the harmonic oscillator. In table 1, we list the parameters for the two Morse potentials shown in figure 1(a). To ensure a fair comparison between anharmonic and harmonic potentials, the parameters in table 1 give the same vibrational frequency $\omega_v = 1838.26$ cm^{-1}, which is representative of the vibrational modes used for light–matter coupling in experiments [21, 26, 45]. The harmonic potential V_C in figure 1 also has the same ω_v.

The electric dipole function along the vibrational coordinate is modeled as [40, 41]

$$\hat{d}(q) = d_0(q - q_0)e^{-(q-q_1)^2/2\sigma^2}, \tag{4}$$

which accurately captures the dipole nature of diatomic and polyatomic molecules, depending on the choice of parameters d_0, q_0, q_1 and σ [21]. The set of dipole parameters used in this work are given in table 1. These are chosen to describe the behavior of non-polar vibrations (d_{NP}), which due to nuclear symmetry have a vanishing dipole moment at equilibrium (q_{eq}), but acquire a finite dipole moment away from the equilibrium geometry. Examples of this behavior include the degenerate CO stretching mode in iron pentacarbonyl [32]. The other dipole behavior of interest corresponds to *polar-right* molecules [41], which have a finite dipole moment at equilibrium that further increases as the mode distance q increases. Examples of this behavior include lithium fluoride [46]. In figure 1(b) we show the dipole functions that correspond to the parameters in table 1. Below we study combinations of these potentials and dipole functions to compute the unitary light–matter interaction dynamics of frequency-driven cavity fields.

2.3. MCTDH unitary polariton propagation

For accurately computing the quantum field statistics of cavity photons subject to ultrafast frequency modulation, we solve the time-dependent Schrödinger equation in coordinate space with a Hamiltonian given by equation (1) using the multi-configurational time-dependent Hartree (MCTDH) method [47, 48], explicitly developed for the accurate and scalable treatment of strongly coupled anharmonic oscillators, as they commonly occur in photochemistry [49]. The MCTDH method has been successfully used to study strong and ultrastrong light–matter coupling of realistic molecules with quantized optical [46, 50] and infrared cavity fields [41, 51].

In MCTDH, the system wave function $\Psi(t)$ is written in continuous coordinate space by the ansatz

$$\Psi(q, x, t) = \sum_{j_q=1}^{n_q} \sum_{j_x=1}^{n_x} A_{j_q j_x}(t)\phi_{j_q}(q, t)\phi_{j_x}(x, t), \tag{5}$$

which is an expansion in products of the molecular basis functions $\phi_{j_q}(q, t)$ and cavity mode functions $\phi_{j_x}(x, t)$. To obtain the results below, we set $n_q = n_x = 12$ and represent the vibrational motion in an uniform grid with $N_q = 721$ grid points on the interval $2.5 < q < 20.5$ Bohr. The cavity mode is described by a harmonic oscillator basis in a uniform grid with $N_x = 361$ grid points along the dimensionless interval $-90 < x < 90$, which is enough to capture the Fock states that participate in the dynamics.

The wavefunction ansatz in equation (5) is inserted in the Schrödinger equation to obtain a set of coupled nonlinear equations for the amplitudes $A_{j_q j_x}(t)$ and one-dimensional functions $\phi_{j_q}(q, t)$ and $\phi_{j_x}(x, t)$, which are solved numerically using Runge-Kutta propagators. Eigenstates of the coupled system Hamiltonian can also be obtained in the MCTDH method via propagation in imaginary time [52], which is used to initialize the coordinate-space wavefunction $\Psi(q, x, t)$ into a Hilbert space vibrational polariton eigenstate [41, 49, 53].

2.4. Cavity field statistics

The study of intensity and field quadrature correlations is used in quantum optics to distinguish classical and non-classical light sources [54]. The normalized intensity correlation at zero delay $g^{(2)}(0)$ is commonly used to identify light sources in which photons are bunched or anti-bunched [55]. This photocounting behavior is quantified by the Mandel Q parameter of the intracavity field, given by [56]

$$Q = \frac{\langle \Delta\hat{n}^2 \rangle - \langle \hat{n} \rangle}{\langle \hat{n} \rangle}, \tag{6}$$

where $\langle \hat{n} \rangle \equiv \langle \hat{a}^\dagger \hat{a} \rangle$ is the expectation value of photon number operator and $\langle \Delta\hat{n}^2 \rangle$ is the photon number variance. For a classical laser source that has a Poissonian photocount distribution, the Mandel parameter is $Q = 0$ [55]. For sub-Poissonian light sources we have $-1 < Q < 0$ (Fock state, squeezed vacuum) and for super-Poissonian sources we have $Q > 0$ (e.g., thermal light, entangled photon pairs).

Quadrature squeezing is an alternative metric for characterizing quantum light sources. This is done by comparing the variances of the electric field quadratures $\hat{x} = (\hat{a} + \hat{a}^\dagger)$ and $\hat{y} = -i(\hat{a} - \hat{a}^\dagger)$ relative to the vacuum Fock state [55]. For vacuum, the normalized quadrature variances are $\langle \Delta\hat{x}^2 \rangle = \langle \Delta\hat{y}^2 \rangle = 1$. Quadrature squeezing implies that $\langle \Delta\hat{x}^2 \rangle < 1$ or $\langle \Delta\hat{y}^2 \rangle < 1$, i.e., one of the quadratures components has less quantum noise than the standard vacuum. In terms of the generalized phase space quadrature $\hat{X}_\theta = \cos\theta\,\hat{x} + \sin\theta\,\hat{y}$, the squeezing factor (in dB) is defined as $\zeta_\theta = -10 \times \log \langle \Delta X_\theta^2 \rangle$ [57], where θ is a phase space angle that can be experimentally tuned using homodyne techniques. We only consider cases with $\theta = 0$ and $\theta = \pi/2$ in this article.

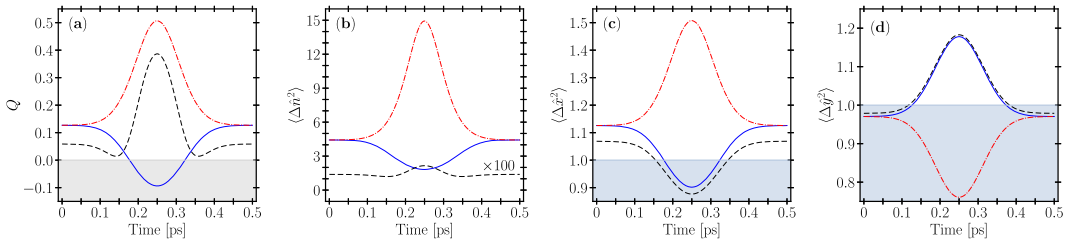

Figure 2. Ground state in ultrastrong coupling under frequency modulation. (a) Evolution of the Mandel Q parameter for a polar-right vibration with a blue modulation of the cavity frequency ($\eta = +0.2$, solid line), a polar-right vibration in red detuning ($\eta = -0.2$, dot-dashed line) and a non-polar vibration in blue detuning ($\eta = +0.2$, dashed line). The shaded region indicates sub-Poissonian photocount statistics. (b) Evolution of the photon number variance $\langle \Delta \hat{n}^2 \rangle$ for the three cases in panel a. The curve for non-polar vibrations is rescaled by 100. (c) Evolution of the quadrature variance in the phase space direction $\theta = 0$. (d) Evolution of the quadrature variance at $\theta = \pi/2$. In panels c and d, the shaded region indicates squeezing relative to the standard vacuum. The light–matter coupling parameter is $\lambda_g = 0.2$. Throughout this work, the frequency modulation pulse is centered at 250 fs and is 147 fs wide (FWHM).

3. Cavity frequency modulation in ultrastrong coupling

In this section we study the evolution of the Mandel Q parameter, the cavity number variance $\langle \Delta \hat{n}^2 \rangle$, and the generalized quadrature variance $\langle \Delta X_\theta^2 \rangle$ of the intracavity field $\hat{a}$, for a coupled vibration-cavity system with a photon frequency modulated according to equation (2). The ultrastrong coupling regime is assumed ($\lambda_g > 0.1$) for a system initialized in the ground state $|\Psi_G\rangle$ or the lower polariton state $|\Psi_{LP}\rangle$ prior to the modulation pulse. We compare the unitary cavity field evolutions obtained for different types of dipole functions and different signs of the peak modulation parameter η. In section 4, a similar analysis is carried out for a strong coupling scenario ($\lambda_g \ll 0.1$).

3.1. Initial ground state

In figure 2 we show the evolution of the Mandel Q parameter, number variance, and quadrature variances at $\theta = 0$ and $\pi/2$, for a coupled vibration-cavity system that is initially in the ground state $|\Psi_G\rangle$ before modulation. The Rabi coupling parameter is $\lambda_g = 0.2$ and the cavity is initially on resonance with the fundamental vibration frequency ω_v. Three cases are highlighted, differing in the type dipole function $d(q)$ and peak frequency shift η: polar-right vibration with blue cavity detuning ($\eta > 0$); polar-right vibration with red cavity detuning ($\eta < 0$), and non-polar vibration with blue cavity detuning ($\eta > 0$). We use the Morse potential V_A in table 1 in all cases.

Figure 2 shows that without frequency modulation, the ground state for polar-right vibrations is slightly super-Poissonian ($Q \approx 0.1$), the number variance is relatively large (≈4.5 photons), there is no squeezing in the x-direction, and the y-quadrature is only weakly squeezed ($\zeta_{\pi/2} = 0.13$ dB) for the chosen λ_g. For non-polar vibrations, the ground state behaves qualitatively similar to the polar-right case, but the number variance is two orders of magnitude smaller. Significant differences between polar and non-polar species become more evident under frequency modulation.

For polar-right molecules we find an asymmetry in the evolution of the cavity field observables depending on the sign of the modulation amplitude η. For blue frequency modulations ($\eta > 0$), the ground state becomes transiently sub-Poissonian at the modulation peak (see figure 2(a)), largely driven by a significant decrease of the number variance (see figure 2(b)). The x-quadrature also becomes squeezed by 0.41 dB at the modulation peak (see figure 2(c)), accompanied by the increase in the y-quadrature variance (see figure 2(d)). In contrast, for red modulations ($\eta < 0$) the same polar-right vibrational mode generates a cavity field with super-Poissonian statistics ($Q \approx 0.5$) at the modulation peak, associated with a significant increase in the number variance (see figure 2(b)). The x-quadrature variance grows relative to the modulation-free value, and the conjugate y-quadrature becomes squeezed $\zeta_{\pi/2} = 1.2$ dB at the modulation peak.

In order to understand this behavior, in figure 3 we show the corresponding photocount distributions $P(n)$ before and during the cavity frequency modulation. In figure 3(a), we show the decrease of the average photon number and variance predicted for polar-right molecules at the peak of a blue modulation, relative to the initial coupled ground state. This decrease is responsible for the change in the Q parameter around the Poissonian $Q = 1$ limit in figure 2(a). For comparison, we also show the exact Poissonian distribution for a coherent state with the same average photon number as the system at the modulation peak. For blue modulations the overlap of the driven system with the coherent state distribution can be significant, but for red modulations the deviations from a coherent state are large at low n (see figure 3(b)).

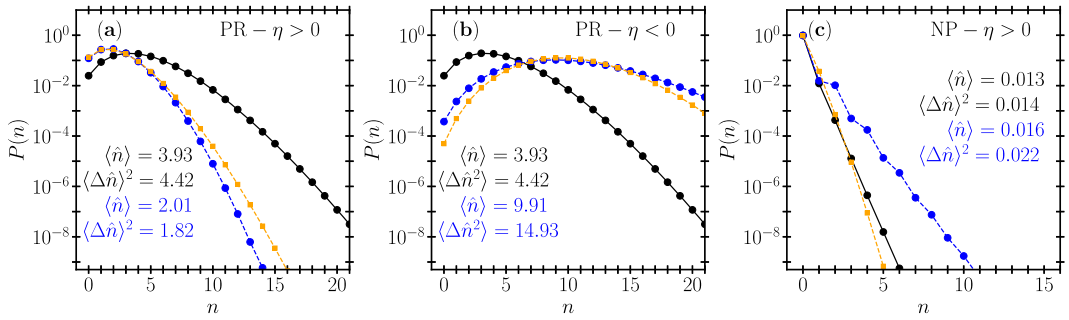

Figure 3. Ground state photocount distribution under frequency modulation. (a) Photon number distribution $P(n)$ before modulation (black line) and the modulation peak (blue line) for a polar-right molecule subject to blue Gaussian frequency modulation ($\eta = +0.2$); (b) $P(n)$ for polar-right molecules with red modulation ($\eta = -0.2$); (c) $P(n)$ for non-polar molecules with blue modulation ($\eta = +0.2$). In all panels, the photon distribution of a coherent state $|\alpha\rangle$ with the same mean photon number as the modulated state at peak detuning is also shown (orange line). The legends indicate the mean photon number and number variance before modulation (black font) and at the modulation peak (blue font). The light–matter coupling parameter is $\lambda_g = 0.2$.

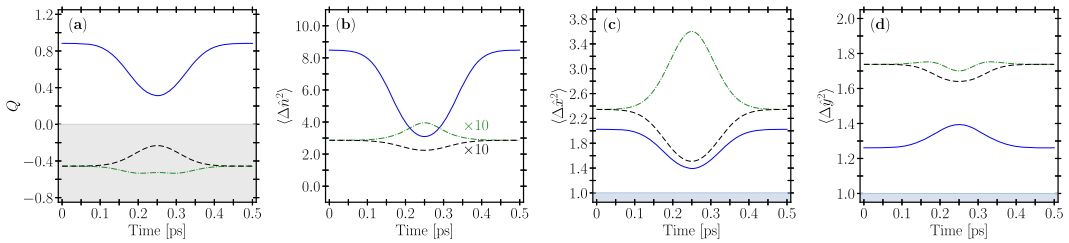

Figure 4. Lower polariton in ultrastrong coupling under frequency modulation. (a) Evolution of the Mandel Q parameter for a polar-right vibration with a blue modulation of the cavity frequency ($\eta = +0.2$, solid line), a non-polar vibration with red modulation ($\eta = -0.2$, dot-dashed line) and a non-polar vibration with blue modulation ($\eta = +0.2$, dashed line). The shaded region indicates sub-Poissonian photocount statistics. (b) Evolution of the photon number variance $\langle \Delta \hat{n}^2 \rangle$ for the three cases in panel a. The curve for non-polar vibrations is rescaled by 10. (c) Evolution of the quadrature variance in the phase space direction $\theta = 0$. (d) Evolution of the quadrature variance at $\theta = \pi/2$. In panels c and d, the shaded region indicates squeezing relative to the standard vacuum. The light–matter coupling parameter is $\lambda_g = 0.2$.

The $P(n)$ distributions for non-polar vibrations with and without frequency modulation are shown in figure 3(c). Without modulation, the photon number and number variance of the coupled ground state are orders of magnitude smaller than the case of polar vibrations. This is consistent with previous works [40, 41]. Despite the small absolute numbers, figure 3(c) shows that the photocount distribution broadens at the peak of a blue modulation shown, which explains the increase of the number variance in figure 2(b).

3.2. Initial lower polariton

We now carry out the analysis from the previous section on a coupled system that is initialized in the lower polariton state $|\Psi_{\mathrm{LP}}\rangle$ at ultrastrong coupling ($\lambda_g = 0.2$). Excited polariton population is commonly produced in non-linear cavity infrared spectroscopy experiments [21]. We again study polar-right and non-polar vibrations under blue frequency modulation, but now also analyze the dynamics of non-polar molecules under red modulation ($\eta = -0.2$).

Figure 4(a) shows that lower polariton state for $\lambda_g = 0.2$ is super-Poissonian ($Q \approx 0.85$) for polar-right molecules and sub-Poissonian for non-polar vibrations ($Q \approx -0.45$). The number variance is large for polar-right vibrations (≈ 8.5 photons), but is an order of magnitude smaller for non-polar species (see figure 4(b)). Moreover, there is no squeezing in the x- or y-quadrature in either case. Under pulsed frequency modulation, the cavity observables vary significantly for the molecular species considered, although the sign of the Mandel Q parameter does not change for the pulse parameters used. In contrast with the ground state analysis in section 3.1, frequency modulating the lower polariton does not generate squeezing at the modulation peak (see figures 4(c) and (d)). The corresponding photocount distributions with and without modulation are shown in figure 5. The deviation of the number distribution from a classical coherent state is more notorious for both polar and non-polar species. For non-polar vibrations, figures 5(b) and (c) show that the frequency modulation mainly changes the contribution of low-n Fock states.

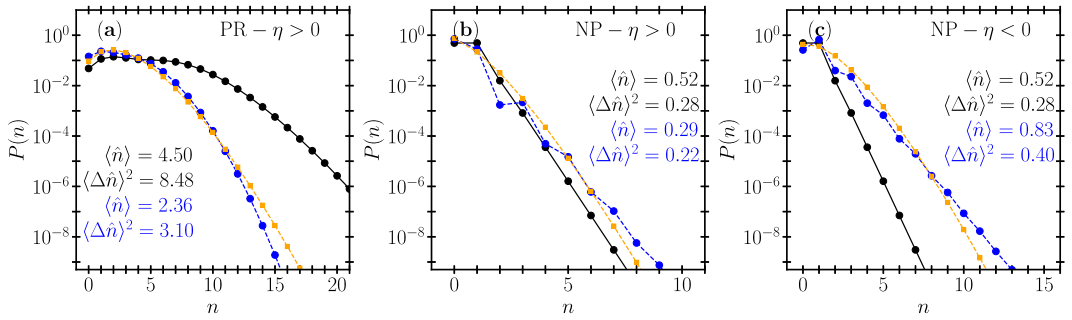

Figure 5. Lower polariton photocount distribution under frequency modulation. (a) Photon number distribution $P(n)$ before modulation (black line) and the modulation peak (blue line) for a polar-right molecule subject to blue Gaussian frequency modulation ($\eta = +0.2$); (b) $P(n)$ for non-polar molecules with blue modulation ($\eta = +0.2$); (c) $P(n)$ for non-polar molecules with red modulation ($\eta = -0.2$). In all panels, the photon distribution of a coherent state $|\alpha\rangle$ with the same mean photon number as the modulated state at peak detuning is also shown (orange line). The legends indicate the mean photon number and number variance before modulation (black font) and at the modulation peak (blue font). The light–matter coupling parameter is $\lambda_g = 0.2$.

4. Non-adiabatic excitations in vibrational strong coupling

In section 3 we studied the ultrastrong coupling regime of equation (1) by setting $\lambda_g = 0.2$. For the Morse potential V_A (see table 1), this corresponds to the Rabi coupling strength $g_{10} = \lambda_g \omega_{10} \approx 360$ cm^{-1} and a Rabi splitting of 973 cm^{-1} in linear transmission for polar-right vibrations (greater than $2g_{10}$). Although such splitting magnitudes are currently beyond experimental reach with Fabry–Perot resonators [32], expected improvements in mid-infrared resonator technology may facilitate ultrastrong coupling studies in the near future [33].

In this section we explore the cavity field statistics subject to a photon frequency modulation under strong coupling conditions, which are experimentally accessible with current resonator technology [19, 20]. For this we set $\lambda_g \sim 10^{-2}$, corresponding to Rabi splittings no greater than 300 cm^{-1}. The main qualitative difference expected in strong coupling is that the polariton spectrum can have energy gaps ΔE that are comparable with the bandwidth of modulation pulse $\Delta\omega = 2\sqrt{2\ln 2}/\tau$. For the modulation pulse assumed in this work ($\tau = 62.5$ fs) the bandwidth is $\Delta\omega = 226.6$ cm^{-1}. Whenever an eigenstate state that has a nearby energy gap comparable or smaller than $\Delta\omega$ is driven in frequency, non-adiabatic excitations can be expected to remain in the system after the pulse is over [58].

We illustrate this effect in figure 6, where we compare the evolution of the Mandel Q parameter a vibration-cavity system initialized either in the ground state (figure 6(a)) or the lower polariton eigenstate (figure 6(b)) before the modulation pulse. The coupling parameter is $\lambda_g = 0.08$, which would give a Rabi splitting of 288 cm^{-1} in linear transmission. Curves are shown for polar-right and non-polar vibrations under red and blue modulations ($\eta = \pm 0.2$).

Figure 6(a) shows that an initial ground state evolves in a qualitatively similar way to the ultrastrong coupling case in figure 2(a), with small differences in the values of Q before and during the modulation pulse. The driven wavefunction returns adiabatically to initial ground state after the pulse is over ($t \approx 0.5$ ps), because the energy gap ΔE to the first excited (lower) polariton level (1648 cm^{-1} for polar-right vibrations) far exceeds the modulation bandwidth $\Delta\omega$. In other words, no residual post-pulse excitations remain in the system.

In contrast, figure 6(b) shows that although starting from the lower polariton state can lead to an evolution of the Q parameter with the same trends in figure 4(a) for ultrastrong coupling, the pulse turn-off dynamics is qualitatively different. For $\lambda_g = 0.08$, the energy gap ΔE between the lower and upper polariton (UP) eigenstates is 307 cm^{-1} for polar vibrations and 295 cm^{-1} for non-polar molecules. The latter is not much greater than the modulation bandwidth $\Delta\omega$. We therefore expect the system wavefunction to exhibit non-adiabatic excitations after the modulation pulse is over. This manifests in figure 6(b) in an oscillatory behavior of the Mandel Q parameter as the pulse turns off.

We quantify the non-adiabatic excitations generated on the initial lower-polariton wavefunction in figure 7 for polar-right vibrations under red frequency modulation. Analogue results are found for other dipole functions and values of η. The degree of adiabaticity of the system evolution is quantified by the autocorrelation function $|\langle\Psi(t)|\Psi(0)\rangle|^2$. For an adiabatic pulse modulation, the post-pulse autocorrelation should not differ from unity. Figure 7 shows that this is indeed the case for a driven ground state (solid line), which as mentioned above is associated with a large energy gap to the first

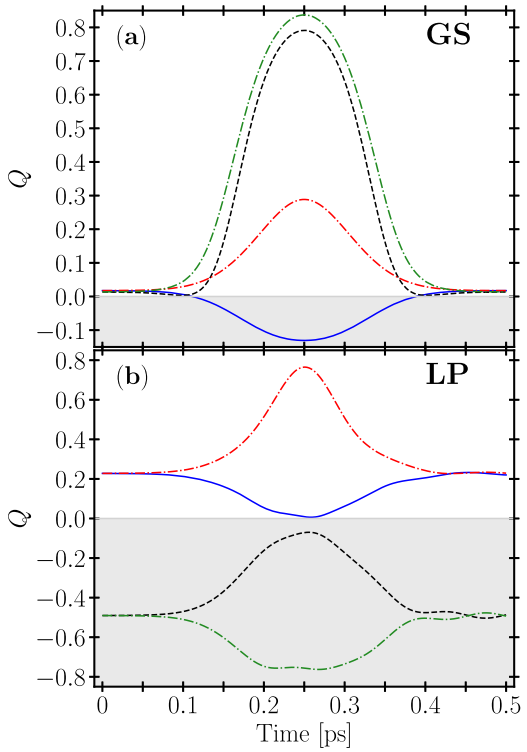

Figure 6. Cavity field statistics in VSC. (a) Evolution of the Mandel Q parameter for a vibration-cavity system initialized in the ground state. (b) Coupled system initialized in the lower polariton state. In all panels, curves correspond to a polar-right vibration with blue modulation ($\eta = +0.2$, solid blue line) and red modulation ($\eta = -0.2$, dot-dashed red line) of the cavity frequency, and for a non-polar vibration with blue detuning ($\eta = +0.2$, dashed black line) and red detuning ($\eta = -0.2$, dot-dashed green line) respect to the undriven cavity frequency. The shaded region indicates sub-Poissonian statistics. The light–matter coupling parameter is $\lambda_g = 0.08$.

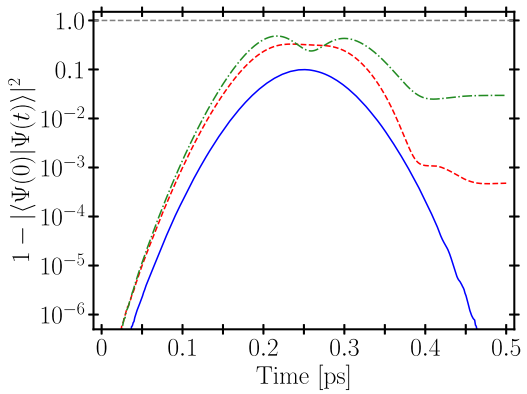

Figure 7. Non-adiabatic dynamics in VSC. State autocorrelation for a polar-right vibration subject to cavity frequency modulation for a system initialized in the ground state (solid line), the lower polariton for $\lambda_g = 0.08$ (dashed line) and the lower polariton with $\lambda_g = 0.05$ (dot-dashed line).

excited polariton level ($\Delta E/\Delta\omega \approx 7.3$). In contrast, for a driven lower polariton state the post-pulse autocorrelation ($t \geqslant 0.5$) can be significantly different from unity, depending on the magnitude of the Rabi splitting. For example, while for $\lambda_g = 0.08$ the system wavefunction is left with about 0.1% of non-adiabatic excitations after the pulse is over (see figure 7, dashed line), for $\lambda_g = 0.05$ the residual population outside the lower polariton after the pulse is over is already a few percent (figure 7, dot-dashed line), which is feasible to detect in nonlinear infrared spectroscopy [21]. This non-adiabatic excitations occur due to the small energy gap between the lower and UP levels, relative to the modulation bandwidth ($\Delta E/\Delta\omega \approx 0.83$ for polar right vibrations).

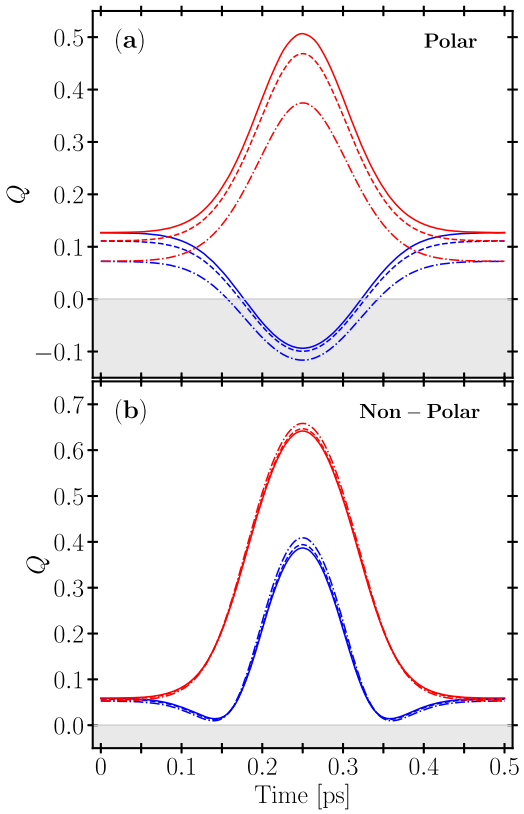

Figure 8. Cavity field statistics and vibrational anharmonicity. (a) Evolution of the Mandel Q parameter for a vibration-cavity system initialized in the ground state for a polar-right vibration. (b) Evolution of the Q parameter for non-polar vibrations. In both panels, curves correspond to a molecular system with Morse potentials V_A (solid lines) and V_B (dashed lines), and the harmonic potential V_C (dot-dashed lines). Red lines correspond to frequency modulations with $\eta = -0.2$ and blue lines to $\eta = +0.2$.

5. Dependence on the vibrational anharmonicity

Molecular vibrations can in principle have similar electric dipole behavior $d(q)$ but differ in the spectral anharmonicity of the nuclear potential. Here we explore the evolution of the Mandel Q parameter in ultrastrong coupling ($\lambda_g = 0.2$), for the same frequency modulation in the previous sections. We compare the Morse potentials V_A and V_B in table 1, which have the same fundamental frequency ω_v but different anharmonicity parameters. The latter is quantified by the anharmonic shift $\Delta_{21} \equiv \omega_v - \Delta E_{21}$, where ΔE_{21} is the energy gap between the $v = 1$ and $v = 2$ vibrational levels. For V_A we have $\Delta_{21} = 32$ cm^{-1} and for V_B we have $\Delta_{21} = 22$ cm^{-1}. For comparison we also consider the purely harmonic case ($\Delta_{21} = 0$). We focus on a system initialized in the ground state, but similar conclusions are found for excited initial states.

In figure 8(a) we show the evolution of the Q parameter for polar-right molecules in ultrastrong coupling. The curves for V_A under blue modulation (blue solid line) and red modulation (red solid line) of the cavity frequency simply reproduce the results in figure 2(a). Reducing the anharmonicity does not qualitatively change the dynamics of the field statistics, i.e., the state can still shift from super-Poissonian to sub-Poissonian for blue modulations ($\eta = 0.2$), but the magnitude of the changes are slightly different. For example, the ground state Q parameter before modulation follows the same hierarchy as the degree of anharmonicity, i.e., $Q_A > Q_B \geqslant Q_{HO}$, where Q_{HO} is the harmonic oscillator limit of the ground state at this value of λ_g. The figure also shows that the relative variations $\Delta Q/Q$ at the modulation peak relative to the initial state, are fairly insensitive to the anharmonicity parameter Δ_{21}. Additional calculations carried out over a broader range values of Δ_{21} confirm this statement.

Figure 8(b) finally shows that at least for a frequency-modulated ground state, no significant dependence with the spectral anharmonicity is expected for the evolution of the Q parameter for non-polar molecular vibrations. These results are consistent with previous works [40, 41], which show that light–matter systems with non-polar molecules are similar to two-level systems and harmonic oscillators with vanishing permanent dipole moments.

Table 2. Summary of predicted cavity field statistics variations. Values of the Mandel Q parameter and squeezing factor ζ_θ (in dB) at $t = 0$ and $t = t_d$ for different dipole moment functions $d(q)$, initial states $|\Psi(0)\rangle$ and cavity frequency modulations ($\eta = \pm 0.2$), in the VUSC regime with the light–matter coupling $\lambda_g = 0.2$. PR and NP correspond to a polar-right and non-polar vibrations, respectively. GS and LP correspond to ground and lower polariton states, and the positive and negative sign of η represent blue and red modulation, respectively.

Case	$d(q)$	$\|\Psi(0)\rangle$	η	$Q(0)$	$\zeta_0(0)$	$\zeta_{\pi/2}(0)$	$Q(t_d)$	$\zeta_0(t_d)$	$\zeta_{\pi/2}(t_d)$
i	PR	GS	+	0.13	−0.51	0.13	−0.09	0.45	−0.71
ii	PR	GS	−	0.13	−0.51	0.13	0.51	−1.78	1.18
iii	PR	LP	+	0.88	−3.06	−1.01	0.31	−1.44	−1.44
iv	PR	LP	−	0.88	−3.06	−1.01	1.99	−4.96	−0.40
v	NP	GS	+	0.06	−0.29	0.09	0.38	0.57	−0.73
vi	NP	GS	−	0.06	−0.29	0.09	0.64	−1.37	1.12
vii	NP	LP	+	−0.46	−3.70	−2.40	−0.23	−1.79	−2.15
viii	NP	LP	−	−0.46	−3.70	−2.40	−0.53	−5.56	−2.31

6. Conclusions

We have shown that the quantum statistics of mid-infrared cavity fields can be dynamically controlled with an ultrafast modulation of the cavity frequency over sub-picosecond timescales, by changing the reflectivity of the conducting cavity mirrors using femtosecond UV pulses. For 20% shifts of the cavity frequency at the modulation peak, we predict the expected changes in the photocount and quadrature field statistics of the intracavity field by computing the unitary dynamics of the underlying cavity-vibration polariton Hamiltonian using numerically exact techniques (see section 2). Our analysis focuses on single-molecule infrared cavities for which the radiate and non-radiative relaxation times are much longer than the frequency modulation timescale.

The dynamics of quantum field statistics is described in terms of the shape of electric dipole function, the anharmonicity of the molecular system, light–matter coupling strength, and whether the system is initially prepared in the ground or lower polariton state before the frequency modulation pulse. For a coupled system in the VUSC regime the cavity field dynamics is adiabatic, while under vibrational strong coupling (VSC) non-adiabatic excitations are possible, provided that the energy gap between the lower and UP levels is comparable with the bandwidth of the frequency modulation pulse.

The results obtained in this work are summarized in table 2, where predicted values of the Mandel Q parameter and squeezing factor ζ_θ before the modulation ($t = 0$) and at the modulation peak ($t = t_d$) are given for a single Morse potential (V_A) in ultrastrong coupling ($\lambda_g = 0.2$), for different polarities of the vibrational mode, different initial states, and different cavity frequency modulations. Additional simulations suggest that qualitatively similar results can be expected for smaller peak frequency modulations $|\eta| \lesssim 0.1$.

As a general rule, we find that the dipolar nature of molecular vibrations is more important descriptor of the degree of control that can be expected for the quantum field statistics in mid-infrared cavities than the anharmonicity of vibrational spectrum. We also find that the photon statistics for polar-left vibrations [41] follows the same qualitative behavior with smaller values of Q and ζ_θ than in the case of polar-right species. Similarly, if the UP is considered as the initial state before modulation, the Mandel parameter and squeezing factor behaves similar to the LP case, but the dynamics is reversed, i.e., evolution of the photon statistics under blue modulation for LP corresponds to dynamics with red modulation for the UP and viceversa.

Cavity designs for implementing the proposed scheme would build on reference [59], where the reflectivity of the conducting cavity mirrors is modulated by promoting interband transitions with ultrafast UV pulses. Although the modulation times are longer than what we propose here, UV pulses were recently used to shift the infrared resonance frequency of a semiconducting/insulator nanoresonator nanostructure [39]. For plasmonic resonators, sub-picosecond modulation of the carrier distribution is also possible [60]. Future mid-infrared cavity designs for tunable molecular polariton studies could build on these proof-of-principle demonstrations [61]. Given the potential feasibility of the proposed scheme, our work paves the way for the development of integrated molecule-assisted quantum light sources for applications in quantum metrology and photonic quantum information processing in the mid-infrared frequency range.

Data availability statement

The data that support the findings of this study are available upon reasonable request from the authors.

Acknowledgments

We thank B Simpkins, A Dunkelberger and J Owrutsky for technical discussions. JFT is supported by ANID Postdoctoral Fellowship No. 3200565. FH is supported by ANID – FONDECYT Regular No. 1181743 and ANID – Millennium Science Initiative Program ICN17_012.

References

[1] O'Brien J L, Furusawa A and Vučković J 2009 Photonic quantum technologies *Nat. Photon.* **3** 687
[2] Daiss S, Welte S, Hacker B, Li L and Rempe G 2019 Single-photon distillation via a photonic parity measurement using cavity QED *Phys. Rev. Lett.* **122** 133603
[3] Weiher K, Agudelo E and Bohmann M 2019 Conditional nonclassical field generation in cavity QED *Phys. Rev.* A **100** 043812
[4] Aspelmeyer M, Kippenberg T J and Marquardt F 2014 Cavity optomechanics *Rev. Mod. Phys.* **86** 1391
[5] Sáez-Blázquez R, Feist J, García-Vidal F J and Fernández-Domínguez A I 2018 Photon statistics in collective strong coupling: nanocavities and microcavities *Phys. Rev.* A **98** 013839
[6] Kimble H J 2008 The quantum internet *Nature* **453** 1023
[7] Yu L *et al* 2015 Two-photon interference at telecom wavelengths for time-bin-encoded single photons from quantum-dot spin qubits *Nat. Commun.* **6** 8955
[8] Clark A S, Chekhova M, Matthews J C F, Rarity J G and Oulton R F 2021 Special topic: quantum sensing with correlated light sources *Appl. Phys. Lett.* **118** 060401
[9] Vega A, Saravi S, Pertsch T and Setzpfandt F 2020 Pinhole quantum ghost imaging *Appl. Phys. Lett.* **117** 094003
[10] Zhang J, Itzler M A, Zbinden H and Pan J-W 2015 Advances in ingaas/inp single-photon detector systems for quantum communication *Light Sci. Appl.* **4** e286
[11] Natarajan C M, Tanner M G and Hadfield R H 2012 Superconducting nanowire single-photon detectors: physics and applications *Supercond. Sci. Technol.* **25** 063001
[12] Shields T *et al* 2020 Mid-infrared quantum interference and polarization entanglement *OSA High-Brightness Sources and Light-Driven Interactions Congress 2020 (EUVXRAY, HILAS, MICS)* (Optical Society of America) p MF1C.7
[13] Spitz O, Herdt A, Wu J, Maisons G, Carras M, Wong C-W, Elsäßer W and Grillot F 2021 Private communication with quantum cascade laser photonic chaos *Nat. Commun.* **12** 3327
[14] Yao Y, Hoffman A J and Gmachl C F 2012 Mid-infrared quantum cascade lasers *Nat. Photon.* **6** 432
[15] Gabbrielli T, Cappelli F, Bruno N, Corrias N, Borri S, De Natale P and Zavatta A 2021 Mid-infrared homodyne balanced detector for quantum light characterization *Opt. Express* **29** 14536
[16] Mancinelli M, Trenti A, Piccione S, Fontana G, Dam J S, Tidemand-Lichtenberg P, Pedersen C and Pavesi L 2017 Mid-infrared coincidence measurements on twin photons at room temperature *Nat. Commun.* **8** 15184
[17] Shalabney A, George J, Hutchison J, Pupillo G, Genet C and Ebbesen T W 2015 Coherent coupling of molecular resonators with a microcavity mode *Nat. Commun.* **6** 1
[18] Shalabney A, George J, Hiura H, Hutchison J A, Genet C, Hellwig P and Ebbesen T W 2015 Enhanced Raman scattering from vibro-polariton hybrid states *Angew. Chem., Int. Ed.* **54** 7971
[19] George J, Shalabney A, Hutchison J A, Genet C and Ebbesen T W 2015 Liquid-phase vibrational strong coupling *J. Phys. Chem. Lett.* **6** 1027
[20] Long J P and Simpkins B S 2015 Coherent coupling between a molecular vibration and Fabry–Perot optical cavity to give hybridized states in the strong coupling limit *ACS Photon.* **2** 130
[21] Grafton A B, Dunkelberger A D, Simpkins B S, Triana J F, Hernández F J, Herrera F and Owrutsky J C 2021 Excited-state vibration–polariton transitions and dynamics in nitroprusside *Nat. Commun.* **12** 214
[22] Xiang B, Ribeiro R F, Li Y, Dunkelberger A D, Simpkins B B, Yuen-Zhou J and Xiong W 2019 Manipulating optical nonlinearities of molecular polaritons by delocalization *Sci. Adv.* **5** aax5196
[23] Dunkelberger A D, Spann B T, Fears K P, Simpkins B S and Owrutsky J C 2016 Modified relaxation dynamics and coherent energy exchange in coupled vibration-cavity polaritons *Nat. Commun.* **7** 1
[24] Xiang B, Ribeiro R F, Dunkelberger A D, Wang J, Li Y, Simpkins B S, Owrutsky J C, Yuen-Zhou J and Xiong W 2018 Two-dimensional infrared spectroscopy of vibrational polaritons *Proc. Natl Acad. Sci. USA* **115** 4845
[25] Dunkelberger A D, Davidson R B, Ahn W, Simpkins B S and Owrutsky J C 2018 Ultrafast transmission modulation and recovery via vibrational strong coupling *J. Phys. Chem* A **122** 965
[26] Muller E A, Pollard B, Bechtel H A, Adato R, Etezadi D, Altug H and Raschke M B 2018 Nanoimaging and control of molecular vibrations through electromagnetically induced scattering reaching the strong coupling regime *ACS Photon.* **5** 3594
[27] Metzger B, Muller E, Nishida J, Pollard B, Hentschel M and Raschke M B 2019 Purcell-enhanced spontaneous emission of molecular vibrations *Phys. Rev. Lett.* **123** 153001
[28] Autore M *et al* 2018 Boron nitride nanoresonators for phonon-enhanced molecular vibrational spectroscopy at the strong coupling limit *Light Sci. Appl.* **7** 17172
[29] Folland T G, Lu G, Bruncz A, Nolen J R, Tadjer M and Caldwell J D 2020 Vibrational coupling to epsilon-near-zero waveguide modes *ACS Photon.* **7** 614
[30] Frisk Kockum A, Miranowicz A, De Liberato S, Savasta S and Nori F 2019 Ultrastrong coupling between light and matter *Nat. Rev. Phys.* **1** 19
[31] Forn-Díaz P, Lamata L, Rico E, Kono J and Solano E 2019 Ultrastrong coupling regimes of light-matter interaction *Rev. Mod. Phys.* **91** 25005
[32] George J, Chervy T, Shalabney A, Devaux E, Hiura H, Genet C and Ebbesen T W 2016 Multiple Rabi splittings under ultrastrong vibrational coupling *Phys. Rev. Lett.* **117** 153601
[33] Askenazi B, Vasanelli A, Todorov Y, Sakat E, Greffet J-J, Beaudoin G, Sagnes I and Sirtori C 2017 Midinfrared ultrastrong light-matter coupling for THz thermal emission *ACS Photon.* **4** 2550
[34] Yoo D, de León-Pérez F, Pelton M, Lee I-H, Mohr D A, Raschke M B, Caldwell J D, Martín-Moreno L and Oh S-H 2021 Ultrastrong plasmon–phonon coupling via epsilon-near-zero nanocavities *Nat. Photon.* **15** 125
[35] Dodonov V 2020 Fifty years of the dynamical Casimir effect *Physics* **2** 67

[36] Jun Y C, Gonzales E, Reno J L, Shaner E A, Gabbay A and Brener I 2012 Active tuning of mid-infrared metamaterials by electrical control of carrier densities *Opt. Express* **20** 1903
[37] Panah M E A, Han L, Norrman K, Pryds N, Nadtochiy A, Zhukov A E, Lavrinenko A V and Semenova E S 2017 Mid-IR optical properties of silicon doped InP *Opt. Mater. Express* **7** 2260
[38] Dunkelberger A D *et al* 2018 Active tuning of surface phonon polariton resonances via carrier photoinjection *Nat. Photon.* **12** 50
[39] Dunkelberger A D *et al* 2020 Ultrafast active tuning of the Berreman mode *ACS Photon.* **7** 279
[40] Hernández F J and Herrera F 2019 Multi-level quantum Rabi model for anharmonic vibrational polaritons *J. Chem. Phys.* **151** 144116
[41] Triana J F, Hernández F J and Herrera F 2020 The shape of the electric dipole function determines the sub-picosecond dynamics of anharmonic vibrational polaritons *J. Chem. Phys.* **152** 234111
[42] Andrews D L, Jones G A, Salam A and Woolley R G 2018 Perspective: quantum Hamiltonians for optical interactions *J. Chem. Phys.* **148** 40901
[43] Elsaesser T and Kaiser W 1991 Vibrational and vibronic relaxation of large polyatomic molecules in liquids *Annu. Rev. Phys. Chem.* **42** 83
[44] Morse P M 1929 Diatomic molecules according to the wave mechanics: II. Vibrational levels *Phys. Rev.* **34** 57
[45] Ribeiro R F, Dunkelberger A D, Xiang B, Xiong W, Simpkins B S, Owrutsky J C and Yuen-Zhou J 2018 Theory for nonlinear spectroscopy of vibrational polaritons *J. Phys. Chem. Lett.* **9** 3766
[46] Triana J F, Peláez D and Sanz-Vicario J L 2018 Entangled photonic-nuclear molecular dynamics of LiF in quantum optical cavities *J. Phys. Chem* A **122** 2266
[47] Beck M, Jackle A, Worth G A and Meyer H-D 2000 The multiconfiguration time-dependent Hartree (MCTDH) method: a highly efficient algorithm for propagating wavepackets *Phys. Rep.* **324** 1
[48] Meyer H D, Gatti F and Worth G A 2009 *Multidimensional Quantum Dynamics: MCTDH Theory and Applications* (New York: Wiley)
[49] Vendrell O, Gatti F and Meyer H-D 2007 Full dimensional (15-dimensional) quantum-dynamical simulation of the protonated water dimer: II. Infrared spectrum and vibrational dynamics *J. Chem. Phys.* **127** 184303
[50] Vendrell O 2018 Collective Jahn–Teller interactions through light–matter coupling in a cavity *Phys. Rev. Lett.* **121** 253001
[51] Triana J and Herrera F 2020 Self-dissociation of polar molecules in a confined infrared vacuum *ChemXiv Preprint* (https://doi.org/10.26434/chemrxiv.12702419.v1) (posted online 24 July 2020)
[52] Meyer H-D and Worth G A 2003 Quantum molecular dynamics: propagating wavepackets and density operators using the multiconfiguration time-dependent Hartree method *Theor. Chem. Acc.* **109** 251
[53] Meyer H-D, Quéré F L, Léonard C and Gatti F 2006 Calculation and selective population of vibrational levels with the multiconfiguration time-dependent Hartree (MCTDH) algorithm *Chem. Phys.* **329** 179
[54] Barnett S M and Radmore P 1997 *Methods in Theoretical Quantum Optics* (Oxford: Oxford University Press)
[55] Gerry C and Knight P 2005 *Introductory Quantum Optics* (Cambridge: Cambridge University Press)
[56] Mandel L 1982 Squeezed states and sub-Poissonian photon statistics *Phys. Rev. Lett.* **49** 136
[57] Andersen U L, Gehring T, Marquardt C and Leuchs G 2016 30 years of squeezed light generation *Phys. Scr.* **91** 053001
[58] Sarandy M S, Wu L-A and Lidar D A 2004 Consistency of the adiabatic theorem *Quantum Inf. Process.* **3** 331
[59] Ji H, Zhang B, Wang W, Lv L and Shen J 2018 Ultraviolet light-induced terahertz modulation of an indium oxide film *Opt. Express* **26** 7204 Wang G, Zhang J, Zhang B, He T, He Y and Shen J 2016 Photo-excited terahertz switch based on composite metamaterial structure *The 8th Int. Symp. on Ultrafast Phenomena and Terahertz Waves* (Optical Society of America) p IT2A.1
[60] Brown A M, Sundararaman R, Narang P, Schwartzberg A M, Goddard W A and Atwater H A 2017 Experimental and *ab initio* ultrafast carrier dynamics in plasmonic nanoparticles *Phys. Rev. Lett.* **118** 087401
[61] Simpkins B S, Dunkelberger A D and Owrutsky J C 2021 Mode-specific chemistry through vibrational strong coupling (or a wish come true) *J. Phys. Chem* C **125** 19081